AGU PUBLICATIONS

JGR

Journal of Geophysical Research: Space Physics

RESEARCH ARTICLE
10.1002/2015JA021225

Key Points:
- Developed an automated procedure to extract plasmapause from IMAGE EUV images
- Validate and evaluate results using statistical analysis of 39 intense storms
- Show that plasmasphere dynamics vary systematically with CME-v-CIR driving

Correspondence to:
R. M. Katus,
rkatus@umich.edu

Citation:
Katus, R. M., D. L. Gallagher, M. W. Liemohn, A. M. Keesee, and L. K. Sarno-Smith (2015), Statistical storm time examination of MLT-dependent plasmapause location derived from IMAGE EUV, *J. Geophys. Res. Space Physics*, *120*, 5545–5559, doi:10.1002/2015JA021225.

Received 23 MAR 2015
Accepted 2 JUN 2015
Accepted article online 4 JUN 2015
Published online 22 JUL 2015

Statistical storm time examination of MLT-dependent plasmapause location derived from IMAGE EUV

R. M. Katus[1,2], D. L. Gallagher[3], M. W. Liemohn[1], A. M. Keesee[2], and L. K. Sarno-Smith[1]

[1]Department of Atmospheric, Oceanic and Space Sciences, University of Michigan, Ann Arbor, Michigan, USA, [2]Department of Physics and Astronomy, West Virginia University, Morgantown, West Virginia, USA, [3]Marshall Space Flight Center, NASA, Huntsville, Alabama, USA

Abstract The location of the outer edge of the plasmasphere (the plasmapause) as a function of geomagnetic storm time is identified and investigated statistically in regard to the solar wind driver. Imager for Magnetopause-to-Aurora Global Exploration (IMAGE) extreme ultraviolet (EUV) data are used to create an automated method that locates and extracts the plasmapause. The plasmapause extraction technique searches a set range of possible plasmasphere densities for a maximum gradient. The magnetic local time (MLT)-dependent plasmapause results are compared to manual extraction results. The plasmapause results from 39 intense storms are examined along a normalized epoch storm timeline to determine the average plasmapause L shell as a function of MLT and storm time. The average extracted plasmapause L shell follows the expected storm time plasmapause behavior. The results show that during the main phase, the plasmapause moves earthward and a plasmaspheric drainage plume forms near dusk and across the dayside during strong convection. During the recovery phase, the plume rejoins the corotationally driven plasma while the average plasmapause location moves farther from the Earth. The results are also examined in terms of the solar wind driver. We find evidence that shows that the different categories of solar wind drivers result in different plasmaspheric configurations. During magnetic cloud-driven events the plasmaspheric drainage plume appears at the start of the main phase. During sheath-driven events the plume forms later but typically extends further in MLT.

1. Introduction

The plasmasphere is the region of high-density (typically between hundreds and thousands of cubic centimeters) and relatively cool (less than 10 eV) plasma corotating with the Earth. The plasmasphere is defined by this colder plasma, which comprises the bulk of the plasma mass within the inner magnetosphere (within approximately 7 R_E of the Earth) and hence influences several significant space environment processes [e.g., *Lemaire and Gringauz*, 1998; *Liemohn*, 2006]. The plasmasphere is torus shaped and extends from the top of the ionosphere out to the plasmapause. The main source of plasmaspheric plasma is the ionosphere. During a period of days the plasma builds up until the concentration reaches equilibrium, when as much plasma flows into the dayside ionosphere as flows out the nightside.

The plasmapause is defined as the outer boundary of the plasmasphere, but there are several methods to determine its location. One method of defining the location of the plasmapause is at the last closed equipotential that is the boundary between corotating and convecting magnetospheric plasma. Earthward of the plasmapause the plasma approximately corotates with the Earth. Outside of this region, the plasma is swept sunward by magnetospheric convection [e.g., *Parks*, 1991]. While this method is useful when describing a simplified picture of plasmaspheric dynamics, this definition is only valid during steady state conditions. This condition rarely if ever exists and is not used in data analysis.

When working with experimental data, the plasmapause can be defined as a specific density value [e.g., *Chappell et al.*, 1970; *Chappell*, 1974], a specific density drop [e.g., *Moldwin et al.*, 2002; *O'Brien and Moldwin*, 2003], or a visually identified gradient in the EUV intensity [e.g., *Goldstein et al.*, 2002; *Goldstein et al.*, 2003]. *Carpenter and Anderson* [1992] modeled the radial extent of the plasmapause as a function of the maximum *Kp* in the previous 24 h. *Larsen et al.* [2007] determined the location of the plasmapause using Imager for Magnetopause-to-Aurora Global Exploration (IMAGE) EUV equatorial density maps using a semiautomated procedure and the *Carpenter and Anderson* [1992] definition. They concluded that future work should provide the plasmapause position as a function of magnetic local time (MLT).

During the main phase of a geomagnetic storm, magnetospheric convection increases and the boundary between the corotating and convecting plasma moves earthward [e.g., *Carpenter and Anderson*, 1992; *Moldwin et al*., 2002]. The thermal ions in this outer region, beyond the shrunken plasmapause, are convected sunward by the cross-tail electric field. This increased sunward magnetospheric convection associated with geomagnetic storms forms the plasmaspheric drainage plume [e.g., *Carpenter et al*., 1993; *Grebowsky*, 1971]. During the recovery phase of the storm, the plasmasphere begins to refill and return to equilibrium while the plasmaspause reforms away from the Earth [e.g., *Carpenter*, 1970].

Goldstein et al. [2003] manually determined the plasmapause location for the month of June 2001 using IMAGE EUV data assuming the plasmapause to be the outermost sharp edge where the brightness of the He^+ emissions drops off abruptly at a given magnetic local time (MLT). While this method produces relatively accurate results, it does have some problems, including being time consuming and meticulous. Sources of error with this method include the possibility of bias caused by visualization choices. Still, several studies have used manual extractions to examine plasmasphere dynamics [e.g., *Goldstein et al*., 2003; *Liemohn et al*., 2004, 2006; *Sandel et al*., 2003; *Spasojević et al*., 2003; *Gallagher et al*., 2005; *Ridley et al*., 2014]. To get the plasmapause location for long periods of time requires the development and application of an automated method. This could yield plasmapause locations from a large set of storm intervals, which would allow a statistical analysis of plasmaspheric dynamics as a function of storm drivers.

There are two main types of geomagnetic storm drivers in the solar wind: corotating interaction regions (CIRs) and interplanetary coronal mass ejections (ICMEs) [e.g., *Zhang et al*., 2007a, 2007b]. A CIR is composed of high-speed solar wind originating from a solar coronal hole. This structure forms near the leading edge of a high-speed stream, where the stream interacts with the preceding slower solar wind. An ICME is composed of a compressed sheath, ejecta from the corona, or some combination of the two structures. In a sheath (SH), the solar plasma is heated and compressed; on the other hand, in ejecta, the plasma is rarefied and the interplanetary magnetic field (IMF) is large. Geomagnetic storms driven by both SHs and CIRs are associated with a rapidly varying IMF and high dynamic pressure. ICME-driven solar wind may also contain magnetic cloud (MC) structures. MC-driven storms are associated with a strong magnetic field that is rotated through a large angle [e.g., *Klein and Burlaga*, 1982; *Lepping et al*., 1995; *Mulligan and Russell*, 1998; *Lynch et al*., 2003; *Zhang et al*., 2004].

Zhang et al. [2007a, 2007b] created a list of all of the intense ($Dst_{peak} \leq -100$ nT) storms that occurred during solar cycle 23. Each of the storms was categorized by its solar wind driver as being a CIR or ICME. The ICME-driven events were then subgrouped as sheath, magnetic cloud, or complex structure driven.

Several studies have explored the effects of ICMEs versus CIRs. For instance, *Denton et al*. [2006] examined the differences in the plasma sheet for the two types of events. Using the Los Alamos National Laboratory satellites magnetospheric plasma analyzer, they show that the plasma sheet temperature is modulated by CIR-driven events and the plasma sheet density is better modulated by ICME-driven events. *Borovsky and Denton* [2006] identified 21 differences between magnetic cloud-, sheath-, and CIR-driven storms. These differences involve the bow shock, the magnetosheath, the radiation belts, the ring current, the aurora, the plasma sheet, magnetospheric convection, ULF pulsations, spacecraft charging in the magnetosphere, and the saturation of the polar cap potential. Both of these studies show that ICME convection is stronger during the main phase but CIR convection continues after the storm peak.

Huttunen and Koskinen [2004] found that the energy partitioning within geospace during storms driven by solar wind sheath structures, a definition that included both sheaths in front of ICMEs and CIR-driven events, was fundamentally different than ICME-driven intervals because of the high dynamic pressure and fluctuating upstream conditions. *Lu* [2006] and *Turner et al*. [2009] focused on the recovery phase of storms, concluding that CIR storms are substantially more geoeffective than ICME-driven events.

Numerical models have also been used to investigate the difference between ICME and CIR storms. In particular, there have been quite a few inner magnetospheric modeling studies examining the ring current response to these two driver structures [e.g., *Jordanova*, 2006; *Liemohn and Jazowski*, 2008; *Jordanova et al*., 2009; *Liemohn et al*., 2010; *Liemohn and Katus*, 2012; *Katus et al*., 2015]. The consensus view is that CIR-driven storms are significantly different from ICME-driven storms. This is true even for sheath-driven ICME storms. The solar wind structure during the main phase of an SH storm is similar to that during the main phase of a CIR storm, with high dynamic pressure and fluctuating IMF. The resulting storms, however, differ in many significant ways, as noted in these studies.

A few studies have noted similarities between ICME- and CIR-driven storms. For instance, using global magnetohydrodynamic (MHD) modeling, *Ilie et al*. [2010a, 2010b] found that the magnetosphere acts as a low-pass filter, damping the influence of variations of less than an hour, during both kinds of driving conditions. *Liemohn et al*. [2011, 2013] also examined MHD numerical results and noted that the near-Earth nightside current systems follow a similar systematic timing and intensity variation throughout the storm sequence regardless of driver structure.

Even with the large list of comparisons between storms driven by ICMEs and CIRs, there has been very little done regarding similarities or differences in plasmaspheric dynamics during such events. A large part of this dearth of analysis is the lack of an automated yet robust procedure for identifying the plasmapause in IMAGE EUV observations.

This study describes the development of a simple automated procedure to extract the plasmapause location from IMAGE EUV data using the basic definition of the plasmapause as the radial distance with the sharpest density gradient at each MLT. The MLT-dependent plasmapause results during intense ($Dst_{\text{peak}} \leq -100$ nT) geomagnetic events that occurred between the years 2000 and 2002 are presented. These results are then compared with manually extracted plasmapause location data. The extracted plasmapause results are also generalized and validated using normalized superposed epoch analysis. The plasmapause results are then used to statistically examine the question: Do solar wind driving conditions alter storm time plasmasphere dynamics? This study shows evidence that the plasmapause dynamics are different for ICMEs driven by magnetic clouds and sheaths. In particular, the plasmaspheric drainage plume forms at the earlier for magnetic cloud-driven events but extends further in L shell and MLT for sheath-driven events.

2. Method

The plasmasphere has been globally imaged by the Imager for Magnetopause-to-Aurora Global Exploration (IMAGE) spacecraft. The IMAGE spacecraft completed an elliptical polar orbit, with apogee and perigee altitudes of 7.2 R_E and 1000 km, respectively, every 14.2 h. The apogee began at 40° north geographic latitude. It then precessed to 90° during the first year of the mission (directly over the North Pole) and back to 40° during the second year. The IMAGE mission applied a variety of imaging techniques to produce the first comprehensive global view of the plasma populations, which made it possible to observe the large-scale dynamics of the magnetosphere.

The IMAGE extreme ultraviolet (EUV) imager detects resonantly scattered solar EUV photons with a wavelength of 30.4 nm that have been resonantly scattered by singly ionized helium [*Sandel et al*., 2000]. The sizeable database of IMAGE global snapshots from the extreme ultraviolet (EUV) imager provides revolutionary observations of spatial and temporal plasma distributions throughout the plasmasphere. In this study, the IMAGE EUV data have been mapped to the equator using the approach detailed in *Gallagher et al*. [2005]. The appendix of that work describes the conversion of photon counts from the EUV imager into column-integrated density and the mapping of these values, using the assumption of a dipole magnetic field, into the geomagnetic equator. The resulting estimates of the He^+ densities were found to have a varying uncertainty in absolute value that is not expected to significantly influence the location of distinct density structures found in the images, such as the plasmapause. An example of the mapped EUV data is shown in Figure 1. In this figure, IMAGE EUV data are mapped to the equatorial plane, the Sun is to the left, and the axis extends 6 R_E at midnight, 06:00, noon, and 18:00 MLT. The data also show several plasmaspheric features and the axes that will be used in this study, labeled for easy reference.

IMAGE EUV data have some issues that become sources of error in identifying the plasmapause. One main concern is that the photon accumulation time varies across each of the three cameras in the direction transverse to the spacecraft spin direction. This accumulation time variation results in a composite image with fewer counts and more noise at the two opposite edges and with pairs of "stripes" at the camera head borders. The camera heads overlap by 3°, creating a local increase in counts at the midline between heads and lower counts on either side. A second concern that arises when extracting the plasmapause is the occurrence of lower counts near local midnight. This lower photon accumulation problem arises primarily because Earth obscures UV light from the Sun and will be referred to as an Earth's shadow effect.

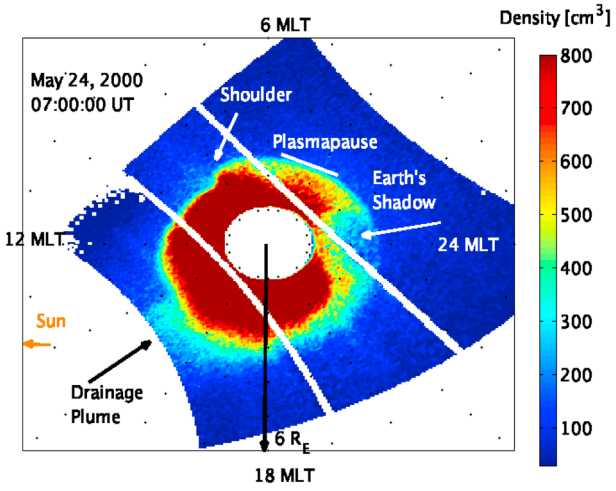

Figure 1. Imager for Magnetopause-to-Aurora Global Exploration (IMAGE) extreme ultraviolet (EUV) data mapped to the equatorial plane with labeled features. Plasmasphere features and axis on 24 May 2000 used in this study. In this type of plot the EUV data are shown in a linear scale that saturates at 800 cm^{-3}.

Another issue that may affect the final result is instrumental photon binning, but this is mostly overcome by applying a flat field correction. Finally, data resolution must be taken into account. While the camera sensitivity is relatively high, higher resolution near the plasmapause would allow a more accurate result. Despite these issues, several studies have used these data to extract the plasmapause location [*Moldwin et al.*, 2002; *Goldstein et al.*, 2003, 2004; *Obana et al.*, 2010].

In this study, the MLT-dependent plasmapause location is determined using a simple automated method. The method defines the plasmapause as the radial distance with the sharpest negative radial He^+ density gradient at each MLT within each usable IMAGE EUV 10 min observation. This technique removes any possibility of subjective bias in manually determined plasmapause data resulting from visualization techniques. Applying the automated procedure also dramatically speeds up the plasmapause identification process.

The automated plasmapause extraction method consists of five steps. In the first step, unusable data are removed. An observation is excluded if the IMAGE EUV snapshot image has less than 20% coverage at any universal time (UT). This includes when the satellite is too close to the equatorial plane, if the satellite is pointing at the Sun and the camera high voltage has been lowered, or if the data have been deemed bad for any other reason during the initial data processing. These observations are not in this analysis. Derived plasmapause locations are also excluded if they fall within two pixels of the two overlapping edges between the three EUV cameras. This exclusion is done during the initial processing of the data. When the data are mapped to the equatorial plane, the two pixels surrounding the camera edges are nullified. This removal is done for every 10 min observation that is examined.

In the second step of the automated plasmapause extraction method, the range of valid radial distances for the plasmapause is defined. That is, the search area is reduced to between 1.5 and 7 R_E. The plasmapause is rarely as close as 1.5 R_E, and if it did, dayglow would interfere with the result. Additionally, during storm time the plasmapause should be closer than 7 R_E [*Chappell et al.*, 1970; *Carpenter and Anderson*, 1992]. Furthermore, plasmapause boundaries tend to be less well defined at distances greater than 7 R_E and thus the sharpest gradient method tends to be ineffective. Therefore, the plasmapause is restricted to L shells between 1.5 and 7 R_E.

In the third step of the automated method, the range of valid He^+ densities for the plasmapause is defined. Specifically, the search area is reduced to between 40 and 800 cm^{-3}. These boundaries extend further than those used in *Chappell et al.* [1970] and *Chappell* [1974]. This range was chosen to remove the possibility of picking a plasmapause location that is too close to the background level [*Goldstein et al.*, 2003] while remaining away from effects caused by airglow close to the Earth.

In the fourth step of the automated method, the largest density gradient at each MLT for each time step (10 min EUV snapshot) is found. The location of the plasmapause is determined using only the maximum value of the radial density gradient for each time step at each 0.01 h MLT. The image is analyzed at each 0.01 h in MLT and 0.25 h of L shell. The MLT resolution is higher than the EUV image resolution, but the grid of the image is not aligned with standard L-MLT coordinates, so this very dense MLT cadence allows a plasmapause calculation that cuts many different ways through the EUV image grid. This oversampling is smoothed later in the process back down to a value close to the EUV image resolution.

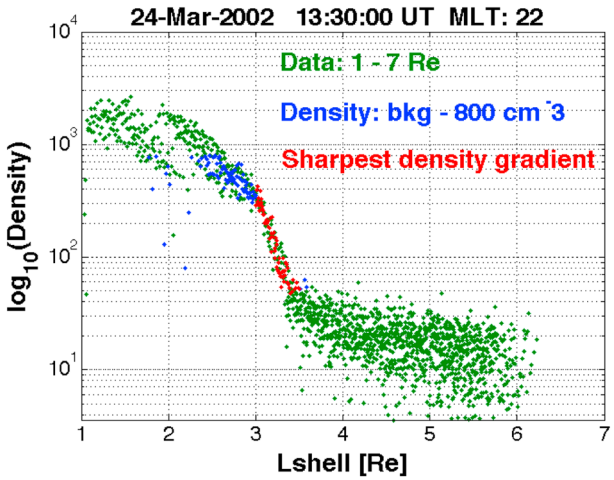

Figure 2. An ideal example of the $\log_{10}$ density versus L shell (R_E) for a 0.5 h bin centered at 22 MLT at 13:30 UT on 24 March 2002.

A result from step four of the automated method is shown in Figure 2. Figure 2 shows an ideal example of density versus L shell at 22 MLT at 13:30 UT. All of the data between 1 and 7 R_E are shown in green, blue, and red. A subset of all of the data that describes the densities between 40 and 800 cm^{-3} is shown in blue and red. A subset of the range of densities with the sharpest gradient across 0.5 R_E is shown in red. While this plot shows a clear plasmapause location, as defined using the sharpest gradient, the result is not always this clear. The results tend to be less clear at MLTs associated with the plasmaspheric drainage plume, the Earth's shadow, and camera edges.

In the fifth step of the automated method, the plasmapause results are filtered. Results are dropped if they are within two pixels of missing data. The remaining MLT-dependent plasmapause positions are then smoothed. To do this, any data outside of the 90th percentile window of the L shell distribution for that UT are removed. A running average in MLT is then completed on the remaining plasmapause location data. This averaging can be done to bin the results in any MLT width. The MLT bin size for the plasmapause location results for several plots shown in the next few sections of this paper is 0.1 h MLT. While this still allows variation in the MLT-dependent plasmapause result, it removes the most extreme outliers and reduces the size of the output.

3. Results

The plasmapause location results for three particular UT during 24 May 2000 are shown in Figure 3. Figure 3 shows the data in a format similar to that of Figure 1. IMAGE EUV data are mapped to the equatorial plane, the Sun is to the left, and the axis extends 6 R_E at midnight, 06:00, noon, and 18:00 MLT. To highlight the plasmapause, the color bar is set up such that the EUV data saturate at 800 cm^{-3}. Densities larger than 800 cm^{-3} are out of the reasonable range for the plasmapause. The 0.1 h MLT-binned plasmapause location results are shown as red dots.

Figure 3a (at 06:20 UT) shows an exemplary plasmapause result. The sharpest gradient appears to follow what is visually the edge of the He^+ plasmapause, and it transitions relatively smoothly from one MLT to the next. No plasmapause data are given for 15:00 MLT, where the EUV data do not radially extend to the expected location of the plasmapause. The largest jump in this plasmapause result is near local midnight. This region, labeled as the Earth's shadow in Figure 1, is known to cause issues when using the sharpest gradient method. The severity of the error caused by the Earth's shadow is dependent upon the season and the satellite location.

Figure 3b (at 08:40 UT) shows another high-quality plasmapause result. The sharpest gradient falls close to, but outside of, the visual edge of the plasmasphere. This result highlights the difference between the sharpest gradient and visually determined results. The visual location of the plasmapause is highly dependent upon the color scale. Additionally, the sharpest gradient method applied here uses the outermost L shell. In Figure 3b, the plasmapause again appears to transition from one MLT to another fairly smoothly. Similar to Figure 3a, the Earth's shadow again causes some error near local midnight. The main differences between this plot and the plot at 06:20 UT are the development of the plasmaspheric drainage plume and the shoulder. The plume causes some inconsistency in the MLT transitions. This jump

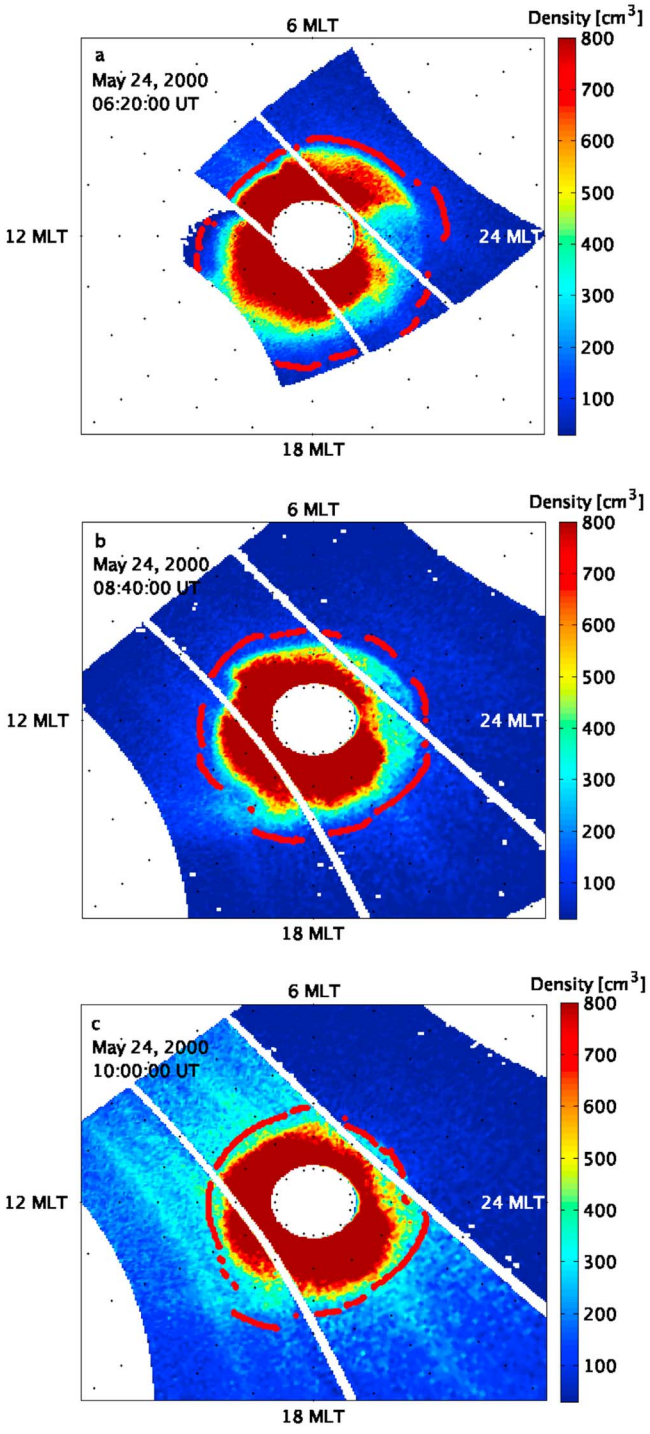

Figure 3. IMAGE EUV data for 3 times during 24 May 2000. The three examples also show the extracted plasmapause location (red dots) found using the automated method. In each plot the EUV data are shown in a linear scale that saturates at 800 cm^{-3}.

is especially evident near 15 MLT. This EUV image has a striking "shoulder" feature visible near 9 MLT. This feature is not seen in the plasmapause result.

One additional effect found in this plot is emphasized by the plasmapause results extending from 19:00 to 24:00 MLT. The EUV data in this region appear smeared or streaky. This effect is caused by the location of the satellite and the technique that maps the EUV data to the equatorial plane, which is another source of error in our results.

Figure 3c (at 10:00 UT) shows a slightly rougher result. The result is not bad; the MLT transition of the plasmapause is relatively smooth all around the plot. The result also extends radially outward where it is expected that the plume should be. Nonetheless, the image has issues. The image shows smearing in the EUV data due to satellite position and the mapping technique as well as the "seam" between the cameras. All of these issues are sources of error in the automated extraction technique.

4. Event Comparison

To quantify the quality of the plasmapause data found using the automated method, these results are compared to data found manually. The method used to find these data is described by *Goldstein et al.* [2003]. They used the "He^+ edge" in IMAGE EUV data to visually determine the plasmapause position. That is, they defined the plasmapause location as the outermost sharp edge where the brightness drops abruptly. Both the automated (red) and manually (black) extracted plasmapause results for 3 times during the 11 August 2000 geomagnetic event are shown in Figure 4. The format of Figure 4 follows that of Figure 3. The IMAGE EUV data are mapped to the equatorial plane, the Sun is to the left, and the axis extends 6 R_E at midnight, 06:00, noon, and 18:00 MLT. The 0.1 h MLT-binned plasmapause location results are shown as red dots, and the manually extracted data are shown as black dots.

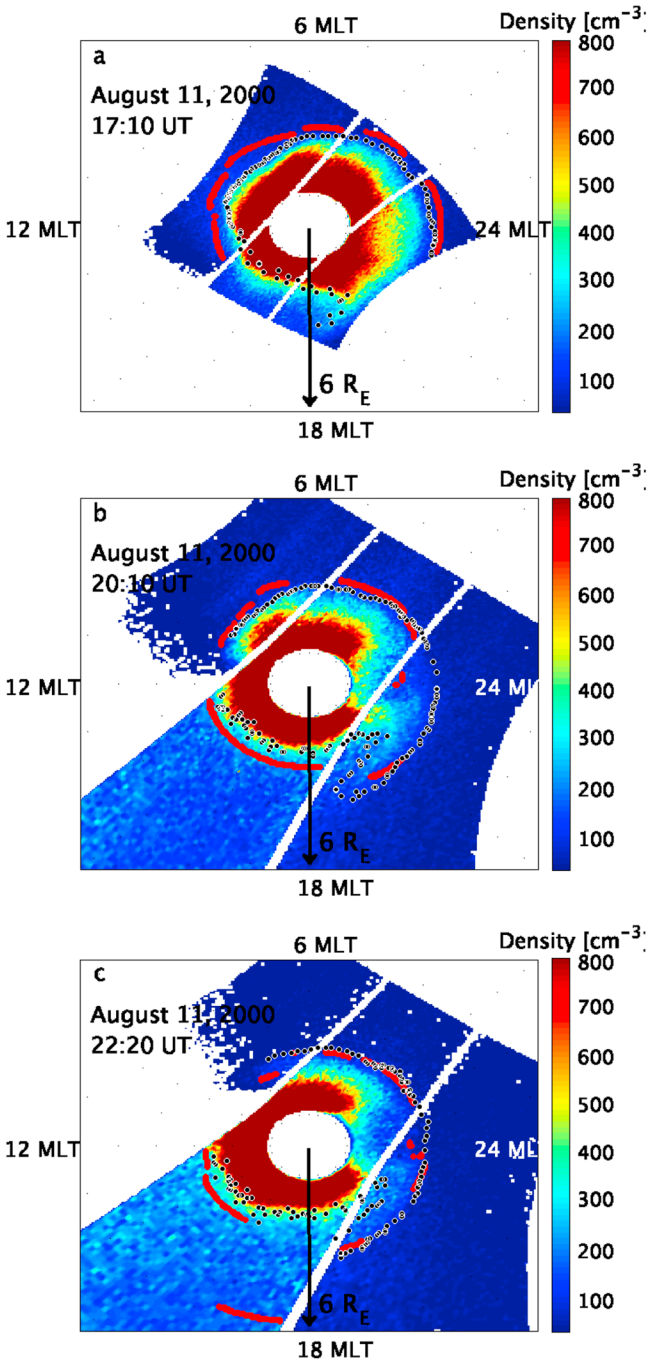

Figure 4. Automated (red dots) plasmapause data compared to manual (black dots) data for 3 times during the 11 August 2000 event. In each plot the EUV data are shown in a linear scale that saturates at 800 cm^{-3}.

Figure 4a (at 17:00 UT) shows a similar plasmapause result using both the manual and automatic extraction methods. The main difference between the two results is that the manually found values tend to be earthward of the automatically extracted locations. Another difference is that the automated method did not determine a plasmapause between 15:00 and 18:00 MLT, while the manually extracted method highlights a drainage plume that is difficult to see with this color bar.

Figures 4b and 4c (at 20:00 and 22:20 UT) again show similar plasmapause results using both the manual and automatic extraction methods. While the manually found edge again appears earthward of the automated plasmapause results, the two methods overlap for several hours of MLT. The largest differences between these two results are near the Earth's shadow and the plasmaspheric drainage plume. The manual results near the Earth's shadow look better than the automatic results in the 20:10 UT plot. Additionally, the manual results follow the inside edge of the drainage plume in the 22:20 UT plot, while the automatic results follow the outside edge in the late afternoon sector.

While the manual plasmapause extractions provide a simple method to assess the quality of the automated extractions, both versions have sources of error. This work shows three example times comparing the two methods, but while conducting this study, the results for all of the available storms and times of overlapping availability were examined. In general, the two methods produce results that are similar but the difference may be as large as 1 R_E. This variation in the results may suggest the effects of visual subjective bias. One major MLT-dependent discrepancy in the two results is the plasmapause near the Earth's shadow. This problem could be addressed in future work for the automated method by applying trigonometry to determine and enhance the data in the affected region. The problem could also be addressed by excluding the data to avoid the issue, but for now the affected data are included. It should also be noted that this work finds it important that the plasmapause location be consistently obtained for statistical use.

Table 1. The Average Storm Phase Duration for Each Solar Wind Driver Configuration

	All (h)	CIR (h)	ICME (h)	MC (h)	Sheath (h)
Main phase	13.4	15.3	13.2	16.3	9.4
Recovery phase	76.7	64.0	78.2	74.0	76.1
Number of storms	39	4	35	13	12

5. Statistical Results

Superposed epoch analysis is a statistical technique that is commonly used to describe the average dynamic behavior associated with a set of events [e.g., *Taylor et al*., 1998; *Liemohn and Katus*, 2012]. This study applies a normalized epoch timeline similar to that used in other recent studies [*Katus et al*., 2013; *Katus and Liemohn*, 2013; *Katus et al*., 2015] to conduct our analysis. The epoch markers are defined starting with the time of the storm peak, as defined by the minimum *Dst*. The end of the recovery phase is then defined as the maximum *Dst* in the 96 h following the storm peak. The beginning of the main phase is defined as the maximum *Dst* in the 24 h before the storm peak. This study does not require a storm sudden commencement. The beginning of the initial phase is defined as the largest increase in *Dst* in the 8 h before the start of the main phase with no minimum required value. Six hours are then concatenated to the start of the initial phase to provide information concerning the preliminary state of the magnetosphere. Examples of storm phases found using this method are given in *Katus et al*. [2013], *Katus and Liemohn* [2013], and *Katus et al*. [2015].

These epoch markers were then used to calculate the average duration of each storm phase for the 39 intense ($Dst_{peak} \leq -100$ nT) geomagnetic storms that occurred between 2000 and 2002. The average duration of each storm phase for each category (as defined by *Zhang et al*. [2007a, 2007b]) of solar wind driver is provided in Table 1. The averages for all storms are consistent with the values found in *Pulkkinen et al*. [2007], *Ilie et al*. [2008], *Katus et al*. [2013], *Katus and Liemohn* [2013], and *Katus et al*. [2015]. The timeline is then normalized using linear interpolation to either stretch or compress the duration of each storm phase to the average duration. Because the mapping to the average phase duration is conducted separately for each phase of each storm, note that it is possible for a storm to have one of its phases compressed while another is stretched.

Normalization of the storm timeline aligns the data by phase. This is beneficial for the present study because it alters the timeline to better correspond all of the observations taken during the prestorm, main, and recovery phases with each other. That is, when the timeline is normalized, the storm convection enhances together and stops together for all storms. This alteration is valid during the main phase but may cause distortions during the recovery phase, where time scales correspond with the corotation period of plasma. A great follow-on study could use only the storm peak to superpose the data. Then one could examine whether the plasmasphere rotation indeed lags behind the Earth's rotation. And if so, what is the difference in rotation speed? This is left as a future investigation.

Figure 5 shows the average plasmapause L shell as a function of MLT, along with averages of IMF in the north-south direction (B_z), *SYM-H*, and solar wind dynamic pressure (P_{dyn}). Each of the plots in Figure 5 is along the normalized epoch timeline. The black vertical lines show the start and end of each storm phase. There are two types of plots in Figure 5. In the first type of plot (Figure 5a), the color bar describes the average plasmapause location in L shell (R_E), the *y* axis has 30 min MLT bins, and the *x* axis has 30 min epoch time bins. In the second type of plot (Figures 5b–5d), the color bar describes the density of data in each bin. For *SYM-H*, B_z, and P_{dyn} the *y* axis contains 100 bins and the *x* axis contains 10 min epoch time bins. The second type of plot also contains black and white overlaid data that provide the mean and median, respectively.

Figure 5a shows the average L shell (R_E) as a function of MLT and storm time. Initially, the average plasmapause L shell is closer to the Earth near local noon. During the main phase, the plasmapause location moves closer to the Earth near local dawn and midnight sectors. This leaves the plume extended away from the Earth near local dusk. Throughout the remainder of the main phase and into the beginning of the recovery phase, the plume can be seen beginning to rotate around the Earth. Through the recovery phase, the plasmapause returns to its initial configuration. Normalizing the timeline potentially obscures corotational signatures in the recovery phase observations, and a comprehensive examination of this aspect of the results is beyond the scope of this main phase-focused study.

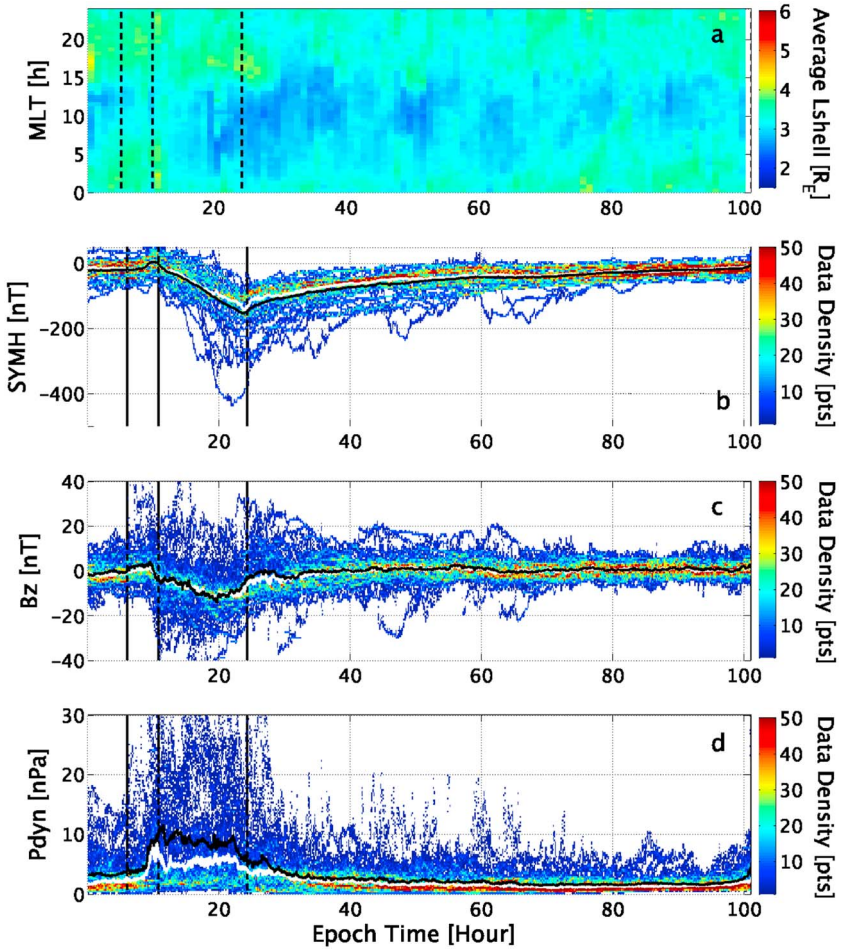

Figure 5. (a) The average plasmapause L shell extracted from IMAGE EUV using the automated method as a function of MLT and normalized epoch storm time for the 39 intense storms that occurred during 2000–2002. The color bar describes the average plasmapause location in 0.5 h (MLT) by 30 min (UT) bins. (b) *SYM-H,* (c) IMF B_z, and (d) solar wind dynamic pressure superposed along the normalized epoch timeline. The black vertical lines show the start or end of each phase. The color describes the density of superposed data in the 100 bins (*y* axis) by 10 min epoch time bins (*x* axis). The black and white overlaid data provide the mean and median, respectively.

The result presented in Figure 5a is consistent with the behavior expected for the plasmapause during solar wind conditions shown in Figures 5c and 5d and storm time described in Figure 5a. The average IMF B_z is negative during the main phase and close to zero throughout the remainder of storm time. The average solar wind dynamic pressure spikes just before the start of the main phase then slowly falls back to its initial value. Furthermore, the average *SYM-H* index can be used to describe the geomagnetic storm associated with these solar wind conditions. The average *SYM-H* has a small peak prior to the main phase then drops to approximately −150 nT at the storm peak and then slowly recovers to initial values.

6. Solar Wind Dependence

Solar wind conditions are known to play a large role in governing the terrestrial magnetic field. This study examines the average automatically extracted plasmapause results as a function of normalized storm time in terms of the solar wind driving condition defined by *Zhang et al*. [2007a, 2007b]. With these results, this study examines whether different solar wind driving conditions alter the plasmaspheric dynamics.

Table 1 shows a primary difference between the all storms and ICME-driven storms categories. That is, the average duration of the main phase of all storms reduces from 13.4 h to 13.2 h for ICME-driven storms while the recovery phase increases from 76.7 h to 78.2 h.

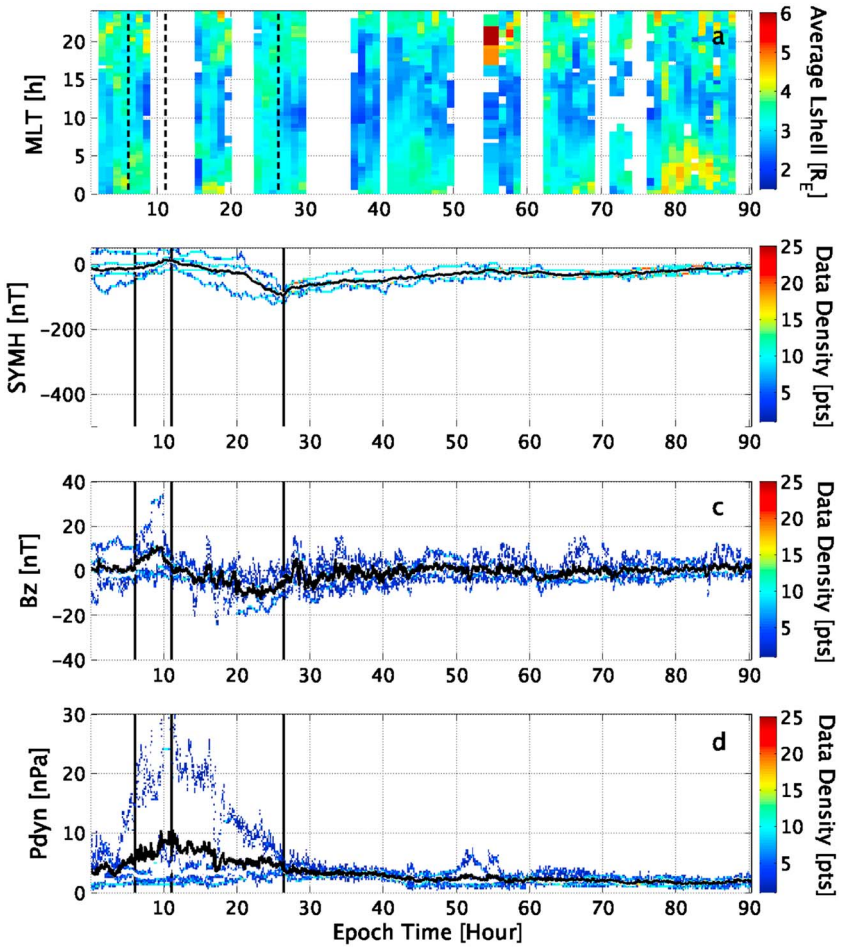

Figure 6. (a) The average CIR-driven plasmapause L shell extracted from IMAGE EUV using the automated method as a function of MLT and normalized epoch storm time for the four intense storms that occurred during 2000–2002. The color bar describes the average plasmapause location in 0.5 h (MLT) by 30 min (UT) bins. (b) *SYM-H* (c) IMF B_z, and (d) solar wind dynamic pressure superposed along the normalized epoch timeline. The black vertical lines show the start or end of each phase. The color describes the density of superposed data in the 100 bins (*y* axis) by 10 min epoch time bins (*x* axis). The black and white overlaid data provide the mean and median, respectively.

Figure 6 is like Figure 5 but for the four intense CIR-driven storms that occurred from 2000 to 2002. The format follows that of previous plots except for one change: the color bar now saturates at 25 data points in Figures 6b–6d. The lower saturation value is because of the lower number of events included in this result. While four storm intervals may not be enough events to provide statistical significance, the average results are still presented.

Examination of the solar wind parameters in Figures 6c and 6d and geomagnetic indices in Figure 6b shows that the storms associated with these four CIRs are all smaller than the average ICME-driven events. Table 1 shows that the average duration of CIR-driven storms has a longer main phase of 15.3 h than ICME-driven storms and a shorter recovery phase (64.0 h).

Figures 7 and 8 show the statistic results for the 12 sheath-driven and the 13 magnetic cloud-driven storms, respectively. The results both follow that of ICME-driven storms. Initially, the plasmapause is closer to Earth near local noon. The plume forms near dusk at the start of the main phase. The plume can then be seen rotating around the Earth for the remainder of the storm. At the start of the main phase, the average plasmapause L shell briefly moves away from the Earth in all MLTs; this behavior resembles the overshielding phenomenon noted by *Goldstein et al.* [2002].

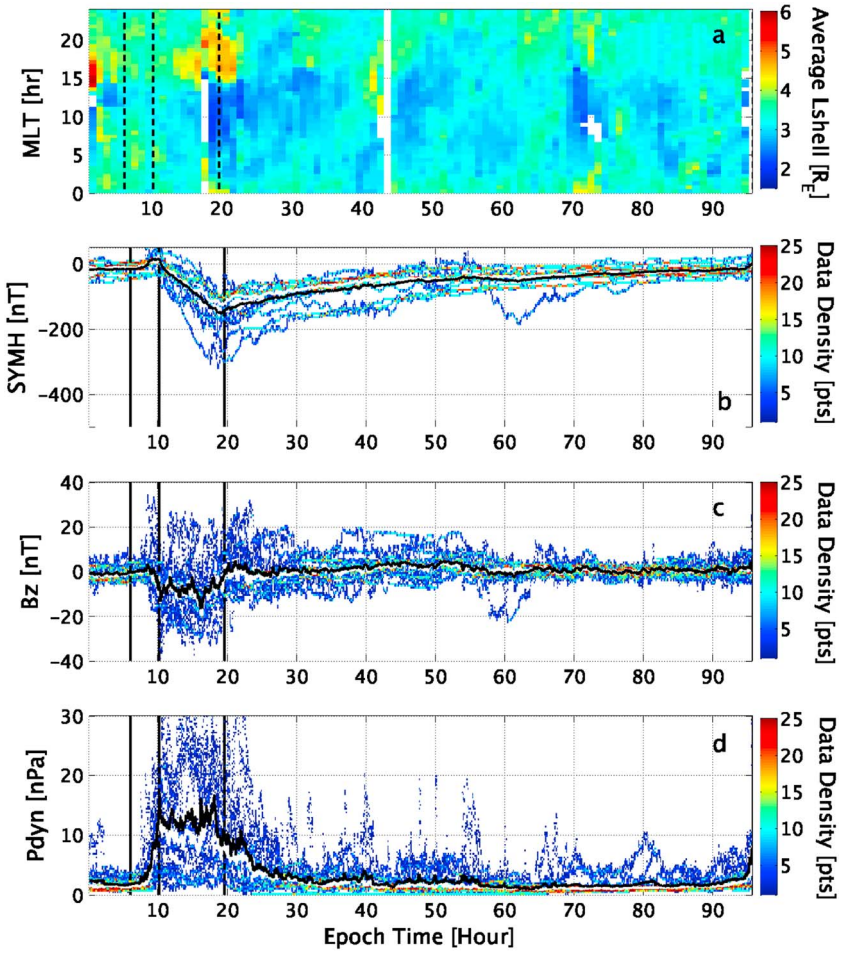

Figure 7. (a) The average sheath-driven plasmapause L shell extracted from IMAGE EUV using the automated method as a function of MLT and normalized epoch storm time for the 12 intense storms that occurred during 2000–2002. The color bar describes the average plasmapause location in 0.5 h (MLT) by 30 min (UT) bins. (b) *SYM-H* (c) IMF B_z, and (d) solar wind dynamic pressure superposed along the normalized epoch timeline. The black vertical lines show the start or end of each phase. The color describes the density of superposed data in the 100 bins (*y* axis) by 10 min epoch time bins (*x* axis). The black and white overlaid data provide the mean and median, respectively.

The average plasmapause is quantified for five distinct storm times in Figure 9. The plots show the median L shell (R_E) versus MLT (h) for each category of solar wind driving at (a) the start of the storm, (b) the beginning of the main phase, (c) 2 h before the storm peak, (d) the peak, and (e) 2 h after the peak. Initially, the plasmapause ranges between approximately 2.75 and 4 R_E for all types of driving conditions. The plasmapause is slightly closer to Earth near local noon. Differences between plasmapause locations for each driver at the start of the initial phase are due to preconditioning.

At the start of the main phase, the plasmapause location is further earthward everywhere except for the plume for magnetic cloud-driven events. At this point we would like to point out that while previous plots have shown the mean, Figure 9 shows the median. Showing the consistent results reveals that the average result is not skewed by any extremes in the data. Additionally, we conducted *t* tests to determine that the means for the different drivers are statistically different across almost all MLTs, the exception only being at MLT near the median intersections (e.g., Figure 9b at 18 and 22 MLT). *T* tests were used to validate each of the similarities and differences listed below.

Two hours before the peak of the storm, the plasmapause is at smaller L shells for all storm drivers but the dynamics are quite different. CIR-driven storms have a more circular plasmapause with a less pronounced plume structure in the afternoon-evening sector than do the various categories of ICME-driven storms.

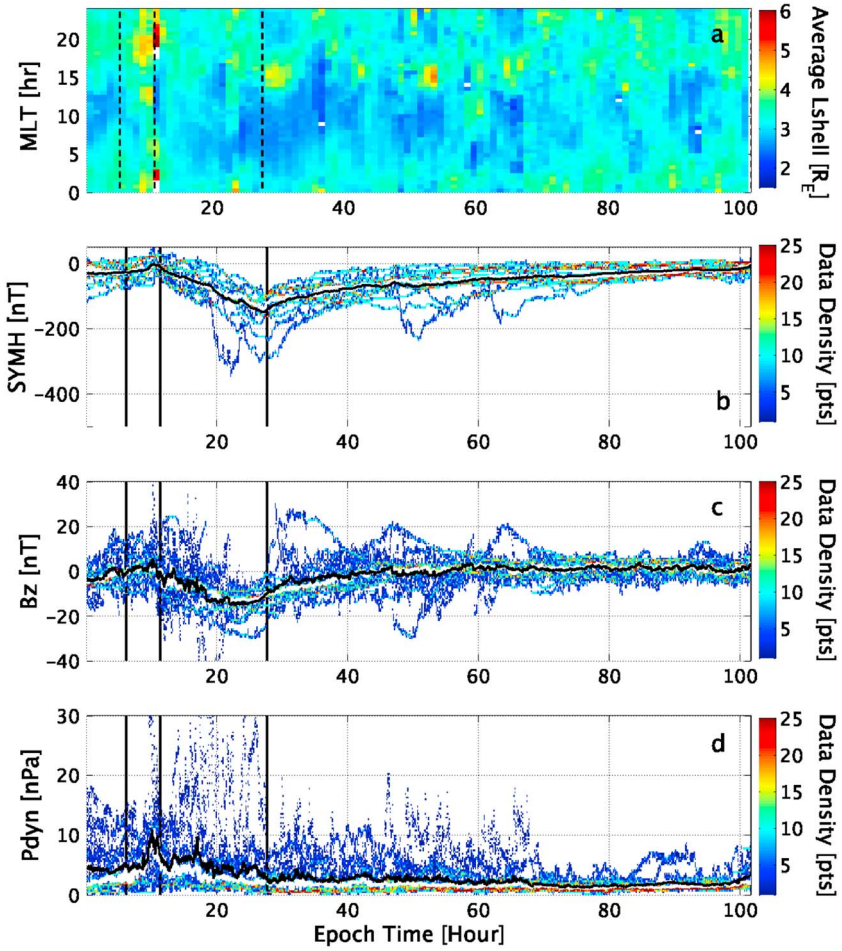

Figure 8. (a) The average magnetic cloud-driven plasmapause L shell extracted from IMAGE EUV using the automated method as a function of MLT and normalized epoch storm time for the 13 intense storms that occurred during 2000–2002. The color bar describes the average plasmapause location in 0.5 h (MLT) by 30 min (UT) bins. (b) *SYM-H* (c) IMF B_Z, and (d) solar wind dynamic pressure superposed along the normalized epoch timeline. The black vertical lines show the start or end of each phase. The color describes the density of superposed data in the 100 bins (*y* axis) by 10 min epoch time bins (*x* axis). The black and white overlaid data provide the mean and median, respectively.

That is, the plasmapause remains between 2.75 and 3.75 R_E for all MLTs. Conversely, all ICME-driven storm categories have a plasmapause that is further earthward around the dayside then sharply extends away from the Earth near dusk. In particular, sheath-driven events have a much more pronounced plume than any other type of driver. The sheath-driven plume is detected farther from Earth and extends further in MLT.

At the storm peak, the average plasmapause L shell for CIR-driven storms is much closer to that of the ICME-driven events around the dayside. Additionally, a plume develops near dusk for the CIR-driven events. Two hours after the peak, the plume begins to become less prevalent.

7. Discussion and Conclusion

This study presents an automated procedure developed to extract the MLT-dependent plasmapause location from Imager for Magnetopause-to-Aurora Global Exploration (IMAGE) extreme ultraviolet (EUV) data from the years 2000 to 2002. The procedure uses a basic definition of the plasmapause. The results are presented for several specific times during two intense geomagnetic events. For one of these events the results are also compared to manually extracted plasmapause results.

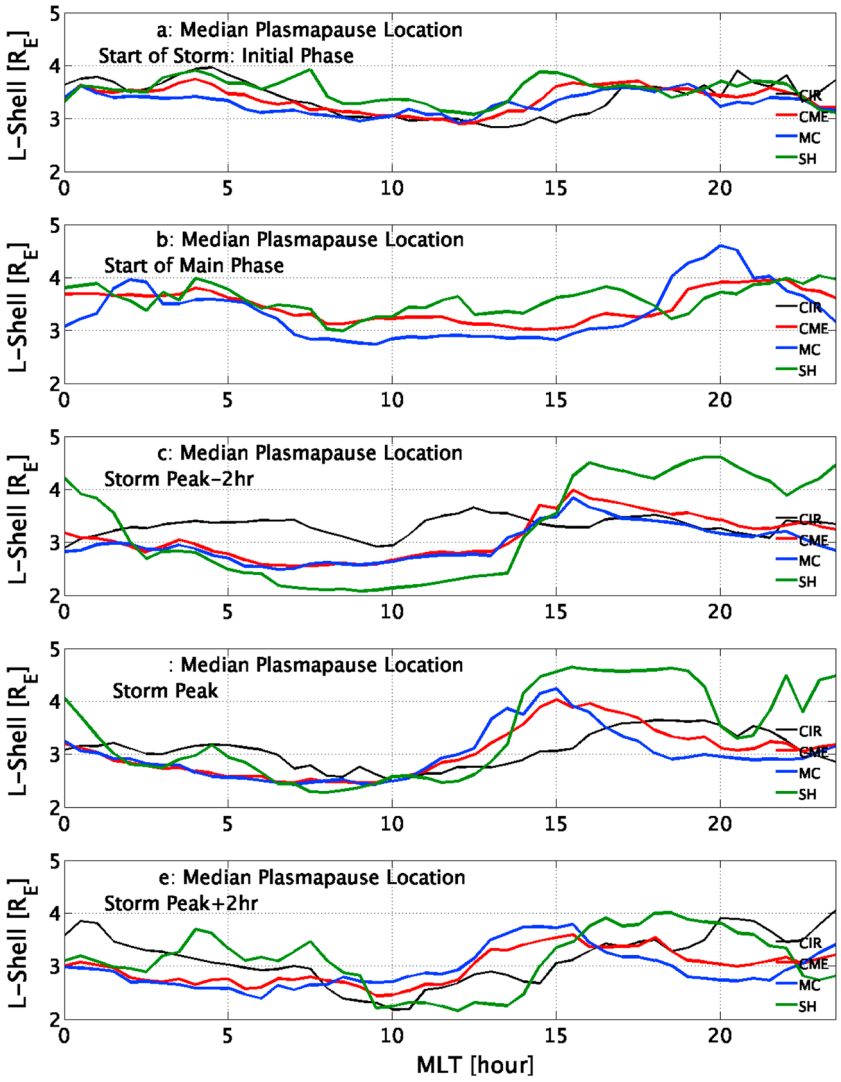

Figure 9. The average plasmapause L shell (R_E) as a function of MLT (h) at (a) the beginning of the storm, (b) the beginning of the main phase, (c) 2 h before the storm peak, (d) the storm peak, and (e) 2 h after the storm peak. Each plot shows the average for the CIR-driven (black), CME-driven (red), magnetic cloud-driven (blue), and sheath-driven (green) storms.

The automatically extracted plasmapause location results are validated by comparison to manually extracted locations. While the manually found plasmapause data are not definitive, the agreement acts to validate the automated results. Examining the phenomenological pattern in plasmapause motion also validates the results. The results shown in this study agree with the expected plasmapause dynamics [e.g., *Carpenter and Park*, 1973; *Horwitz et al*., 1990; *Goldstein et al*., 2004; *Borovsky and Denton*, 2008]. The results show that during the main phase of geomagnetic storms, the average plasmapause locations move earthward and the plasmaspheric drainage plume forms near the dusk sector. The plume then begins to corotate in MLT with the Earth. The location of the plasmapause then slowly moves back away from the Earth during the recovery phase of the storm.

The example storms shown in Figure 3 highlight the differences between the visually detected plasmapause location and the location detected using the automated method. The automated method is systematically farther from the Earth. Using the plasmapause locations found manually, this distance was determined to be approximately 0.5 R_E. This does not imply that the automated method has an error of 0.5 R_E. It implies that the sharpest gradient is 0.5 R_E outward from the visual plasmapause. Additionally, the automated procedure does not always detect small variations in the radial distance of the plasmapause. This is evident in the result near the shoulder feature.

Before examining the results, it is noted that the Earth's shadow can cause a large error near local midnight. This error is a function of the dipole tilt and the location of the satellite. The dipole tilt can reduce the effect by removing significant portions of the field from the shadow. Additionally, the imager on the satellite being too close to or looking too much in the Sun's direction is a problem as well. Therefore, those results are not analyzed. It is also noted that four CIR-driven events may not be enough to generalize the result with statistical significance.

The plasmapause results were then analyzed as a function of solar wind drivers. The results for magnetic cloud-, sheath-, and CIR-driven storms are presented in Figures 6–9. Comparison between the plasmapause locations for the categories of solar wind drivers shows variation in the strength and timing of convection. Early in the main phase, the plasmapause for magnetic cloud-driven events is closer to the Earth and already has a large plume. Conversely, the plasmapause for sheath-driven storms remains farther from the Earth at the start of the main phase but moves further earthward during continued convection approaching the storm peak. Additionally, the plume associated with sheath-driven events extends further in MLT than any other type of driver.

The plasmasphere contains the bulk of the plasma within the inner magnetosphere and is critical to our understanding of the plasma behavior in the inner magnetosphere. The plasmapause location data derived in this paper can be used for many applications. The authors hope that these data will be used among the community. This data set is available at the Geospace Environment Workshop website (http://www-ssc.igpp.ucla.edu/gemwiki/index.php/Data_and_Models).

Acknowledgments

The authors would like to thank NASA and NSF for funding this research through various grants (specifically from NASA via grants NNX08AQ15G, NNX09AF45G, NNX10AQ34C, and NNX11AO60G and NSF through grants ATM-0802705, ATM-0903596, AGS-1102863, and AGS-1113478), including a NASA Graduate Student Research Program fellowship from Marshall Space Flight Center (grant NNX10AL32H). The authors would also like to thank the Kyoto World Data Center (http://wdc.kugi.kyoto-u.ac.jp/index.html) for providing access to the *Dst* and *SYM-H* indices, CDAWeb (http://cdaweb.gsfc.nasa.gov/istp_public/) for providing access to the solar wind data, and University of Arizona (http://euv.lpl.arizona.edu/euv/) for providing access to the IMAGE EUV data and software. Special thanks go to Peter Chi for his help in making the plasmapause data available on the GEMWiki (http://www-ssc.igpp.ucla.edu/gemwiki/index.php/Data_and_Models).

Alan Rodger thanks Balazs Heilig and one anonymous reviewer for their assistance in evaluating this paper.

References

Borovsky, J. E., and M. H. Denton (2006), Differences between CME-driven storms and CIR-driven storms, *J. Geophys. Res.*, *111*, A07S08, doi:10.1029/2005JA011447.

Borovsky, J. E., and M. H. Denton (2008), A statistical look at plasmaspheric drainage plumes, *J. Geophys. Res.*, *113*, A09221, doi:10.1029/2007JA012994.

Carpenter, D. L. (1970), Whistler evidence of the dynamic behavior of the duskside bulge in the plasmasphere, *J. Geophys. Res.*, *75*, 3837–3847, doi:10.1029/JA075i019p03837.

Carpenter, D. L., and R. R. Anderson (1992), An ISEE/whistler model of equatorial electron density in the magnetosphere, *J. Geophys. Res.*, *97*(A2), 1097–1108, doi:10.1029/91JA01548.

Carpenter, D. L., B. L. Giles, C. R. Chappell, P. M. E. Décréau, R. R. Anderson, A. M. Persoon, A. J. Smith, Y. Corcuff, and P. Canu (1993), Plasmasphere dynamics in the duskside bulge region: A new look at an old topic, *J. Geophys. Res.*, *98*(A11), 19,243–19,271, doi:10.1029/93JA00922.

Carpenter, L. D., and C. Park (1973), On what ionospheric workers should know about the plasmapause-plasmasphere, *Rev. Geophys. Space Phys.*, *11*, 133–154.

Chappell, C. R. (1974), Detached plasma regions in the magnetosphere, *J. Geophys. Res.*, *79*(13), 1861–1870, doi:10.1029/JA079i013p01861.

Chappell, C. R., K. K. Harris, and G. W. Sharp (1970), A study of the influence of magnetic activity on the location of the plasmapause as measured by OGO 5, *J. Geophys. Res.*, *75*(1), 50–56, doi:10.1029/JA075i001p00050.

Denton, M. H., J. E. Borovsky, R. M. Skoug, M. F. Thomsen, B. Lavraud, M. G. Henderson, R. L. McPherron, J. C. Zhang, and M. W. Liemohn (2006), Geomagnetic storms driven by ICME- and CIR-dominated solar wind, *J. Geophys. Res.*, *111*, A07S07, doi:10.1029/2005JA011436.

Gallagher, D. L., M. L. Adrian, and M. W. Liemohn (2005), The origin and evolution of deep plasmaspheric notches, *J. Geophys. Res.*, *110*, A09201, doi:10.1029/2004JA010906.

Goldstein, J., R. W. Spiro, P. H. Reiff, R. A. Wolf, B. R. Sandel, J. W. Freeman, and R. L. Lambour (2002), IMF-driven overshielding electric field and the origin of the plasmaspheric shoulder of May 24, 2000, *Geophys. Res. Lett.*, *29*(16), doi:10.1029/2001GL014534.

Goldstein, J., M. Spasojević, P. H. Reiff, B. R. Sandel, W. T. Forrester, D. L. Gallagher, and B. W. Reinisch (2003), Identifying the plasmapause in IMAGE EUV data using IMAGE RPI in situ steep density gradients, *J. Geophys. Res.*, *108*(A4), 1147, doi:10.1029/2002JA009475.

Goldstein, J., R. A. Wolf, B. R. Sandel, and P. H. Reiff (2004), Electric fields deduced from plasmapause motion in IMAGE EUV images, *Geophys. Res. Lett.*, *31*, L01801, doi:10.1029/2003GL018797.

Grebowsky, J. M. (1971), Time-dependent plasmapause motion, *J. Geophys. Res.*, *76*(25), 6193–6197, doi:10.1029/JA076i025p06193.

Horwitz, J. L., R. H. Comfort, and C. R. Chappell (1990), A statistical characterization of plasmasphere density structure and boundary locations, *J. Geophys. Res.*, *95*, 7937–7947, doi:10.1029/JA095iA06p07937.

Huttunen, K. E. J., and H. E. J. Koskinen (2004), Importance of post-shock streams and sheath region as drivers of intense magnetospheric storms and high-latitude activity, *Ann. Geophys.*, *22*, 1729–1738.

Ilie, R., M. W. Liemohn, M. F. Thomsen, J. E. Borovsky, and J. Zhang (2008), Influence of epoch time selection on the results of superposed epoch analysis using ACE and MPA data, *J. Geophys. Res.*, *113*, A00A14, doi:10.1029/2008JA013241.

Ilie, R., M. W. Liemohn, and A. Ridley (2010a), The effect of smoothed solar wind inputs on global modeling results, *J. Geophys. Res.*, *115*, A01213, doi:10.1029/2009JA014443.

Ilie, R., M. W. Liemohn, J. U. Kozyra, and J. E. Borovsky (2010b), An investigation of the magnetosphere-ionosphere response to real and idealized co-rotating interaction region events through global magnetohydrodynamic simulations, *Proc. R. Soc. London, Ser. A*, *466*(2123), 3279–3303, doi:10.1098/rspa.2010.0074.

Jordanova, V. K. (2006), Modeling the behavior of corotating interaction region driven storms in comparison with coronal mass ejection driven storms, in *Recurrent Magnetic Storms: Corotating Solar Wind Streams*, *Geophys. Monogr. Ser.*, vol. 167, edited by B. Tsurutani et al., pp. 77–84, AGU, Washington, D. C., doi:10.1029/167GM08.

Jordanova, V. K., H. Matsui, P. A. Puhl-Quinn, M. F. Thomsen, K. Mursula, and L. Holappa (2009), Ring current development during high speed streams, *J. Atmos. Sol. Terr. Phys.*, *71*, 1093, doi:10.1016/j.jastp.2008.09.043.

Katus, R. M., and M. W. Liemohn (2013), Similarities and differences in low- to middle-latitude geomagnetic indices, *J. Geophys. Res. Space Physics*, *118*, 5149–5156, doi:10.1002/jgra.50501.

Katus, R. M., M. W. Liemohn, D. L. Gallagher, A. Ridley, and S. Zou (2013), Evidence for potential and inductive convection during intense geomagnetic events using normalized superposed epoch analysis, *J. Geophys. Res. Space Physics*, *118*, 181–191, doi:10.1029/2012JA017915.

Katus, R. M., M. W. Liemohn, E. L. Ionides, R. Ilie, D. Welling, and L. K. Sarno-Smith (2015), Statistical analysis of the geomagnetic response to different solar wind drivers and the dependence on storm intensity, *J. Geophys. Res. Space Physics*, *120*, 310–327, doi:10.1002/2014JA020712.

Klein, L. W., and L. F. Burlaga (1982), Interplanetary magnetic clouds at 1 AU, *J. Geophys. Res.*, *87*(A2), 613–624, doi:10.1029/JA087iA02p00613.

Larsen, B. A., D. M. Klumpar, and C. Gurgiolo (2007), Correlation between plasmapause position and solar wind parameters, *J. Atmos. Sol.-Terr. Phys.*, *69*(3), 334–340.

Lemaire, J., and K. I. Gringauz (1998), *The Earth's Plasmapause*, pp. 350, Cambridge Univ. Press, New York.

Lepping, R. P., et al. (1995), The Wind magnetic field investigation, *Space Sci. Rev.*, *71*, 207–229.

Liemohn, M. W. (2006), Introduction to special section on "Results of the National Science Foundation Geospace Environment Modeling Inner Magnetosphere/Storms Assessment Challenge", *J. Geophys. Res.*, *111*, A11S01, doi:10.1029/2006JA011970.

Liemohn, M. W., and M. Jazowski (2008), Ring current simulations of the 90 intense storms during solar cycle 23, *J. Geophys. Res.*, *113*, A00A17, doi:10.1029/2008JA013466.

Liemohn, M. W., and R. Katus (2012), Is the storm time response of the inner magnetospheric hot ions universally similar or driver dependent?, *J. Geophys. Res.*, *117*, A00L03, doi:10.1029/2011JA017389.

Liemohn, M. W., A. J. Ridley, D. L. Gallagher, D. M. Ober, and J. U. Kozyra (2004), Dependence of plasmaspheric morphology on the electric field description during the recovery phase of the 17 April 2002 magnetic storm, *J. Geophys. Res.*, *109*, A03209, doi:10.1029/2003JA010304.

Liemohn, M. W., A. J. Ridley, J. U. Kozyra, D. L. Gallagher, M. F. Thomsen, M. G. Henderson, M. H. Denton, P. C. Brandt, and J. Goldstein (2006), Analyzing electric field morphology through data-model comparisons of the Geospace Environment Modeling Inner Magnetosphere/Storm Assessment Challenge events, *J. Geophys. Res.*, *111*, A11S11, doi:10.1029/2006JA011700.

Liemohn, M. W., M. Jazowski, J. U. Kozyra, N. Ganushkina, M. F. Thomsen, and J. E. Borovsky (2010), CIR vs. CME drivers of the ring current during intense magnetic storms, *Proc. R. Soc. London, Ser. A*, *466*(2123), 3305–3328, doi:10.1098/rspa.2010.0075.

Liemohn, M. W., D. L. De Zeeuw, R. Ilie, and N. Y. Ganushkina (2011), Deciphering magnetospheric cross-field currents, *Geophys. Res. Lett.*, *38*, L20106, doi:10.1029/2011GL049611.

Liemohn, M. W., D. L. De Zeeuw, N. Y. Ganushkina, J. U. Kozyra, and D. T. Welling (2013), Magnetospheric cross-field currents during the January 6–7, 2011, high-speed stream-driven interval, *J. Atmos. Sol. Terr. Phys.*, *99*, 78–84, doi:10.1016/j.jastp.2012.09.007.

Lu, G. (2006), High-speed streams, coronal mass ejections, and interplanetary shocks: A comparative study of geoeffectiveness, in *Recurrent Magnetic Storms: Corotating Solar Wind Streams*, *Geophys. Monogr. Ser.*, vol. 167, edited by B. T. Tsurutani et al., pp. 97, AGU, Washington, D. C.

Lynch, B. J., T. H. Zurbuchen, L. A. Fisk, and S. K. Antiochos (2003), Internal structure of magnetic clouds: Plasma and composition, *J. Geophys. Res.*, *108*(A6), 1239, doi:10.1029/2002JA009591.

Moldwin, M. B., L. Downward, H. K. Rassoul, R. Amin, and R. R. Anderson (2002), A new model of the location of the plasmapause: CRRES results, *J. Geophys. Res.*, *107*(A11), 1339, doi:10.1029/2001JA009211.

Mulligan, T., and C. T. Russell (1998), Solar cycle evolution of the structure of magnetic clouds in the inner heliosphere, *Geophys. Res. Lett.*, *25*, 2959–2962.

Obana, Y., G. Murakami, I. Yoshikawa, I. R. Mann, P. J. Chi, and M. B. Moldwin (2010), Conjunction study of plasmapause location using ground-based magnetometers, IMAGE-EUV, and Kaguya-TEX data, *J. Geophys. Res.*, *115*, A06208, doi:10.1029/2009JA014704.

O'Brien, T. P., and M. B. Moldwin (2003), Empirical plasmapause models from magnetic indices, *Geophys. Res. Lett.*, *30*(4), 1152, doi:10.1029/2002GL016007.

Parks, G. K. (1991), *Physics of Space Plasmas: An Introduction*, Addison-Wesley, Redwood City, Calif.

Pulkkinen, T. I., N. Partamies, K. E. J. Huttunen, G. D. Reeves, and H. E. J. Koskinen (2007), Differences in geomagnetic storms driven by magnetic clouds and ICME sheath regions, *Geophys. Res. Lett.*, *34*, L02105, doi:10.1029/2006GL027775.

Ridley, A. J., A. M. Dodger, and M. W. Liemohn (2014), Exploring the efficacy of different electric field models in driving a model of the plasmasphere, *J. Geophys. Res. Space Physics*, *119*, 4621–4638, doi:10.1002/2014JA019836.

Sandel, B. R., et al. (2000), The extreme ultraviolet imager investigation for the IMAGE mission, *Space Sci. Rev.*, *91*, 197–242.

Sandel, B. R., J. Goldstein, D. L. Gallagher, and M. Spasojevic (2003), Extreme ultraviolet imager observations of the structure and dynamics of the plasmasphere, *Space Sci. Rev.*, *109*(1–4), 25–46.

Spasojević, M., J. Goldstein, D. L. Carpenter, U. S. Inan, B. R. Sandel, M. B. Moldwin, and B. W. Reinisch (2003), Global response of the plasmasphere to a geomagnetic disturbance, *J. Geophys. Res.*, *108*(A9), 1340, doi:10.1029/2003JA009987.

Taylor, J. R., M. Lester, and T. K. Yeoman (1998), A superposed epoch analysis of geomagnetic storms, *Ann. Geophys.*, *12*, 612–624, doi:10.1007/s00585-994-0612-4.

Turner, N. E., W. D. Cramer, S. K. Earles, and B. A. Emery (2009), Geoefficiency and energy partitioning in CIR-driven and CME-driven storms, *J. Atmos. Sol. Terr. Phys.*, *71*, 1023, doi:10.1016/j.jastp.2008.02.005.

Zhang, J., et al. (2007a), Solar and interplanetary sources of major geomagnetic storms ($Dst \leq -100$ nT) during 1996–2005, *J. Geophys. Res.*, *112*, A10102, doi:10.1029/2007JA012321.

Zhang, J., et al. (2007b), Correction to "Solar and interplanetary sources of major geomagnetic storms ($Dst \leq -100$ nT) during 1996–2005", *J. Geophys. Res.*, *112*, A12103, doi:10.1029/2007JA012891.

Zhang, J.-C., M. W. Liemohn, J. U. Kozyra, B. J. Lynch, and T. H. Zurbuchen (2004), A statistical study on the geoeffectiveness of near-Earth magnetic clouds during high solar activity years, *J. Geophys. Res.*, *109*, A09101, doi:10.1029/2004JA010410.